Heat flux modeling using ion drift effects in DIII-D H-mode plasmas with resonant magnetic perturbations

A. Wingen, O. Schmitz, T. E. Evans, and K. H. Spatschek

Citation: Physics of Plasmas **21**, 012509 (2014); doi: 10.1063/1.4862034
View online: http://dx.doi.org/10.1063/1.4862034
View Table of Contents: http://scitation.aip.org/content/aip/journal/pop/21/1?ver=pdfcov
Published by the AIP Publishing

Heat flux modeling using ion drift effects in DIII-D H-mode plasmas with resonant magnetic perturbations

A. Wingen,[1,2] O. Schmitz,[3] T. E. Evans,[4] and K. H. Spatschek[2]
[1]*Oak Ridge National Laboratory, Oak Ridge, Tennessee 37831, USA*
[2]*Institut für Theoretische Physik, Heinrich-Heine-Universität Düsseldorf, D-40225 Düsseldorf, Germany*
[3]*Institut für Energie und Klimaforschung-Plasma Physik, Forschungszentrum Jülich, 52428 Jülich, Germany*
[4]*General Atomics, P.O. Box 85608, San Diego, California 92186, USA*

(Received 19 September 2013; accepted 27 December 2013; published online 14 January 2014)

The heat flux patterns measured in low-collisionality DIII-D H-mode plasmas strongly deviate from simultaneously measured CII emission patterns, used as indicator of particle flux, during applied resonant magnetic perturbations. While the CII emission clearly shows typical striations, which are similar to magnetic footprint patterns obtained from vacuum field line tracing, the heat flux is usually dominated by one large peak at the strike point position. The vacuum approximation, which only considers applied magnetic fields and neglects plasma response and plasma effects, cannot explain the shape of the observed heat flux pattern. One possible explanation is the effect of particle drifts. This is included in the field line equations and the results are discussed with reference to the measurement. Electrons and ions show different drift motions at thermal energy levels in a guiding center approximation. While electrons hardly deviate from the field lines, ions can drift several centimetres away from field line flux surfaces. A model is presented in which an ion heat flux, based on the ion drift motion from various kinetic energies as they contribute to a thermal Maxwellian distribution, is calculated. The simulated heat flux is directly compared to measurements with a varying edge safety factor q_{95}. This analysis provides evidence for the dominate effect of high-energy ions in carrying heat from the plasma inside the separatrix to the target. High-energy ions are deposited close to the unperturbed strike line, while low-energy ions can travel into the striated magnetic topology. © *2014 AIP Publishing LLC*. [http://dx.doi.org/10.1063/1.4862034]

I. INTRODUCTION

Particle and heat transport phenomena are central problems in many branches of physics. In magnetic fusion devices, such as divertor tokamaks, the protection of plasma-facing wall components from heat and particle overloads is a crucial issue to ensure the operability and desired lifetime of the device. Instabilities at the plasma edge, so called edge localized modes (ELMs),[1] go along with the expulsion of high heat loads, which threaten the wall integrity. The standard operational scenario for the next generation tokamak ITER[2] will be a type-I ELMing H-mode. Power extrapolations for ELMs in ITER show that the plasma facing wall components may suffer from fast erosion or melting.[3] The use of edge stochastization by resonant magnetic perturbations (RMPs) is a possible solution to control these instabilities[4] and beneficially affect the plasma-wall interaction.[5]

Nonlinear effects are generic in plasma physics. Stochastic magnetic field line wandering contributes one important aspect.[6,7] Experimental results from TEXTOR show that in high-magnetic-field-side (HFS) [Fig. 1(a)] limited, circular shaped ohmic, and L-mode operation, the ergodization of the plasma is well described by the vacuum field approximation at high resonant field amplitudes.[8,9] In this situation, it was found that the experimentally observed heat flux patterns[10] resemble the topology of the magnetic footprints and trace the stable and unstable manifolds of the last intact island chain.[11,12] A similar good match is obtained between poloidal plasma structures measured in the plasma edge and the magnetic topology from vacuum field line tracing[13] as well as with the plasma fields calculated with the EMC3-Eirene model.[14] Recent analysis of both, heat and particle fluxes to the Dynamic Ergodic Divertor (DED) target at TEXTOR as well as poloidal structures in the plasma edge has shown, that at low resonant field amplitude, significant screening effects can be observed.[15,16] Plasma screening currents were measured directly, and magnetic reconnection with increasing perturbation amplitude as well as a transition into a vacuum like plasma topology has been investigated. These observations also match the prediction for four-field drift kinetic modeling of the plasma response in conditions similar to those in TEXTOR.[17]

Another aspect of transport is the dynamics of particles across the magnetic field. It is known that in inhomogeneous magnetic fields, particle orbits deviate from the magnetic field lines.[18] In a weakly collisional plasma, charged particles gyrate around the magnetic field lines. Since the gyro-radius scales with the magnetic field strength, the gyro-radii (especially for electrons) are very small compared to the dimensions of the system for magnetic fields of the order 1 T. Because of the curvature and gradients of the magnetic field, the particles drift away from the magnetic surfaces. In the gyro-center (guiding-center) approximation, one averages over finite gyro-radius effects. For integrable situations, the deviations of the drift surfaces from the magnetic KAM (Kolmogorow-Arnold-Moser) surfaces increase with the

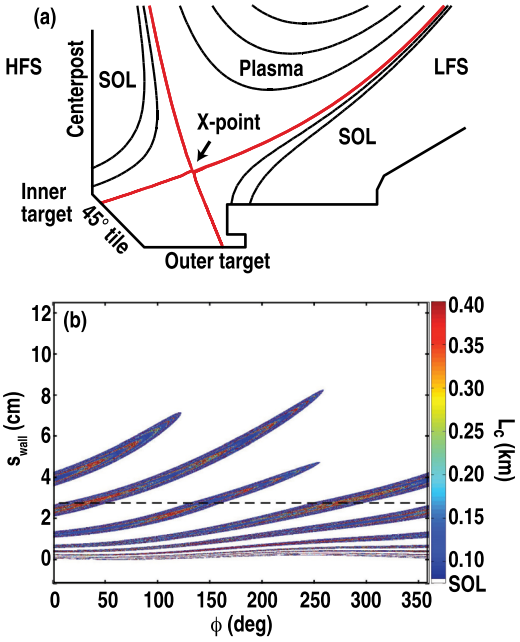

FIG. 1. (a) Sketch of the lower divertor region in a poloidal cross-section of DIII-D. The black curves resemble unperturbed flux surfaces, while the red line is the separatrix. Various parts of the machine are labeled. Acronyms are SOL = scrape-off layer, HFS = high-field-side, LFS = low-field-side. (b) Field line connection length footprint on the inner target of discharge #132 741 at 3000 ms and $q_{95} = 3.81$. The parameter t measures the length along the wall, while $t = 0$ marks the connection of the 45° tile with the vertical centerpost. Using the strike point location t_{SP}, we have $s_{wall} = t_{SP} - t$.

particle energy. The kinetic energy of the particles is therefore, in addition to the perturbation current for the stochastic magnetic field generation, an important parameter for the break-up of drift surfaces.[19]

In DIII-D two specific coil sets, the so-called C-coils and I-coils, have been implemented to enhance core plasma performance and to control the plasma edge transport.[20] Currents flowing in the I-coils create a relatively small magnetic perturbation, which consists mainly of components with toroidal mode number $n = 3$. The C-coils mainly generate modes with $n = 1, 2$ and are often used to compensate for intrinsic error fields which are mainly related to misalignments in the poloidal field coils.

The externally applied RMPs, created by, e.g., the I-coil, cause the ideal separatrix to split into the stable and unstable separatrix manifolds which start oscillating as they approach the x-point.[21–23] The separatrix manifolds represent for the perturbed case the plasma boundary, i.e., three-dimensional last closed flux surfaces (LCFS) exhibiting a helical lobe topology. Their oscillations intersect with the divertor target plates and connect the perturbed plasma volume to the target plates through the helical lobes. Since the separatrix manifolds are the boundary, they determine the shape and position of the field line footprints on the targets, which show a multi-finger striated, helical pattern. The number of helical lobes, i.e., of the resulting striations in the footprint pattern and the overall shape, depends on the actual mode numbers n of the perturbation spectrum.

So, we expect to see, that during the application of RMPs, the divertor heat flux, particle flux, and line emission profiles all change by the spatial splitting of the footprints due to the separatrix manifolds. Such striated heat and particle flux patterns were actually measured during RMP ELM suppression experiments in plasmas for high collisionality ν_e^*[24] in DIII-D[22] ($\nu_e^* > 0.5$) and NSTX[25,26] ($\nu_e^* \geq 1$). This finding was also expected at low ν_e^* from 3D thermal fluid transport modeling with the E3D code[27] and 3D fluid plasma and kinetic neutral transport modeling with EMC3_Eirene.[28] However, in DIII-D experiments with ITER-relevant low collisionality ($\nu_e^* \sim 0.2$), the experimental observations show significant differences between heat and particle flux patterns in the divertor. Although the measurements show similar spatial splitting patterns in terms of contact location on the divertor, that vary systematically with q_{95} (the magnetic safety factor at the $\psi = 0.95$ surface), the heat flux is strongly peaked near the unperturbed strike line position and only has a small heat flux signature as measured in the outer parts of the striated pattern, whereas D_α and CII emission also show prominent bands away from the original intercept with a fair geometrical alignment to the magnetic footprint pattern obtained from vacuum field line tracing.[29] However, in similarly shaped plasmas, but operated in L-mode with moderate neutral beam heating and hence low toroidal rotation, strong heat flux is observed in the outer lobes too.[5] The poorly understood collisionality dependence and the comparison to the TEXTOR results suggest that plasma response effects and drift effects of the hot ions from the interior are likely candidates for the observed heat and particle flux patterns.

In this paper, a drift model is presented to analyze the relevance of ion and electron transport in the hot edge plasma of an H-mode with resonant magnetic perturbations. We will examine the assumption that the bulk of the divertor surface heat flux in ITER-relevant, low-collisionality H-mode plasmas is due to ion bombardment and not electron conduction, and that the drift orbits of the ions make their strike point (SP) insensitive to the effects of the RMP on the magnetic surfaces (unlike the electrons). Thus, heat comes out in one location and particles in another.

The paper is organized as follows. In Sec. II, the experimental measurements of heat and particle flux are presented. Based on the good agreements with L-mode plasmas, a first comparison with vacuum field line modeling is done in Sec. III. Vacuum field line tracing is extended to include particle drift motion in Sec. IV. Numerical results from the drift model are then compared to the measurements in Sec. V. This paper finishes with a summary of conclusions in Sec. VI.

II. HEAT AND PARTICLE FLUX MEASUREMENTS IN H-MODE

In this paper, we compare heat and particle flux patterns for ITER-similar shape, high triangularity plasmas at ITER-relevant low collisionality $\nu_e^* = 0.2$ with modeling from vacuum field line tracing and guiding center particle drift motion. We analyze DIII-D discharge #132 741 with q_{95} ramp down. In this discharge, ELM suppression was obtained in three q_{95} resonant windows, i.e., within $3.2 < q_{95} < 3.9$ interrupted for $3.63 < q_{95} < 3.7$ by three large ELM events and some compound ELM activity.[30] Nevertheless, this wide extension of the resonant q_{95} window provides data for a good

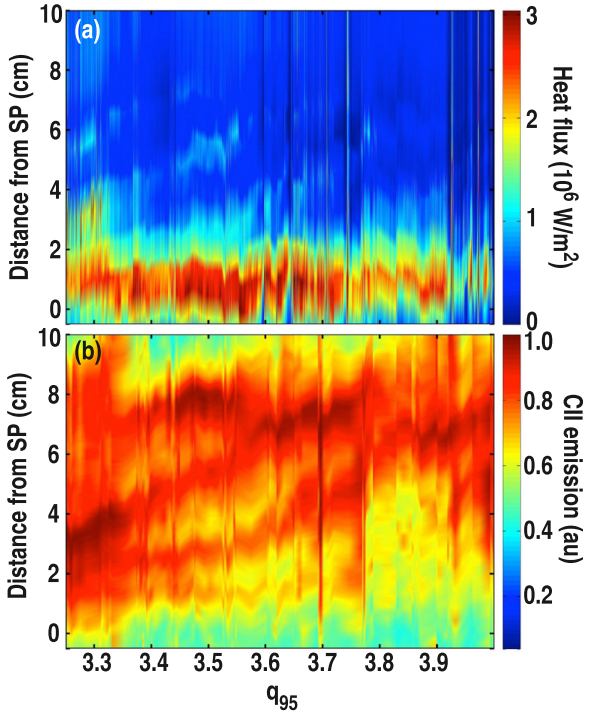

FIG. 2. Heat flux measurement (a) in discharge #132 741 on inner divertor target during ramp down of q_{95} compared with CII emission measurement (b) at same position. The y-axis is the relative distance from the inner SP along the vessel wall.

diagnosis of footprint structures. Note that within the ELM suppressed window, a clear reduction in the pedestal temperature is obtained causing a q_{95} resonant pedestal pressure reduction.[31] This thermal loss from the pedestal will be related to the heat flux patterns in this paper.

The heat flux data shown in Fig. 2(a) were obtained with a fast framing IR camera,[29,32] which can observe radial profiles of the complete inner and outer divertor areas within a toroidal span of $\Delta\phi = 48°$ centered at $\phi = 165°$. An overlapping toroidal region of $\Delta\phi = 30°$ centered at $\phi = 150°$ is observed simultaneously using a CCD camera with a set of filters suitable to get spectral lines strongly related to the incoming particle flux, here measured as CII intensity, shown in Fig. 2(b). Note that the CII measurement is integrated along the line of sight and contains, besides the actual particle flux to the target, the upstream emission from within the scrape-off layer (SOL). Typically though, CII only exists up to 1–2 cm away from the target plate, it is assumed that the CII emission is strongly related to the particle flux at the target. CII emissions are qualitatively similar to the D_α emissions, as discussed in Ref. 29. Both figures focus on the inner target region only and show the pattern extend along the vessel wall, given by the distance s_{wall} from the inner, former unperturbed, SP, as a function of q_{95}. Due to the outer strike point position in the considered discharge, the camera view of the outer strike point is obscured by wall elements around the pump, so there is no data available for the outer target.

Both measurements show a striation, which is geometrically similar in both cases, from the applied RMP. The striation pattern itself is formed due to the q_{95} ramp and will be discussed in more detail later on (Fig. 3). Nevertheless, both

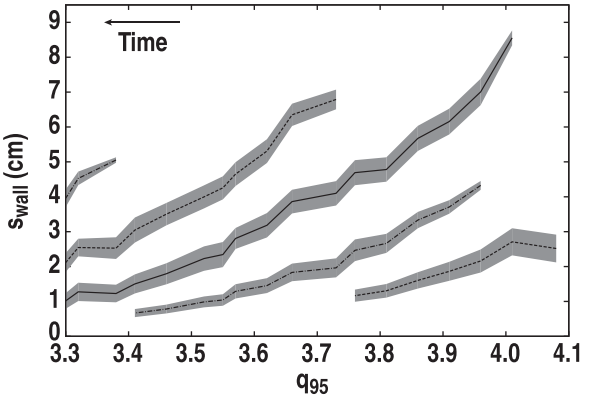

FIG. 3. Position and width of field line connection length footprint fingers with changing q_{95} in discharge #132 741 at fixed toroidal angle of $\phi = 150°$. The different lines mark the position of the respective finger's center, while the grey area shows the area covered by the respective finger. Each line style, either solid, dashed, or dotted-dashed, represents a different finger of the footprint. Note that two fingers appear discontinuous at different locations due to the toroidal periodicity, but are actually the same fingers. Note that the discharge progresses in time from right to left here.

measurements differ significantly from each other with respect to the relative signal strength of the striations. In the heat flux, the main peak remains more or less fixed at the SP position, while the striation pattern is at least three times weaker. The CII emission on the other hand generates a strong striation pattern with only a very weak emission signal at the SP location. This suggests that the particle flux is much higher in the outer lobes relative to the SP location. The heat flux shows the exact opposite behavior.

Figure 4 shows heat flux and D_α intensity profiles, measured in discharge #129 194 at $t = 3000$ ms during complete ELM suppression.[29,32] The measurement of D_α intensity is obtained with a D_α filter at $\lambda = 656.6$ nm with a width of $\Delta\lambda = 10$ nm observing perpendicular to the surface of the 45° tile at the inner divertor. This allows integration of the largest fraction of the localized line emission. Hence, the D_α intensity, although it is a line integrated measurement, can be used as a reasonable approximation for the distribution of the target particle flux. In this discharge, similar features are detected as seen in discharge #132 741. The heat flux is almost entirely deposited as one large peak, located at the SP position, $s_{wall} = 0$, while the D_α intensity reveals the typical RMP striation. Only a very small heat deposition in the outer

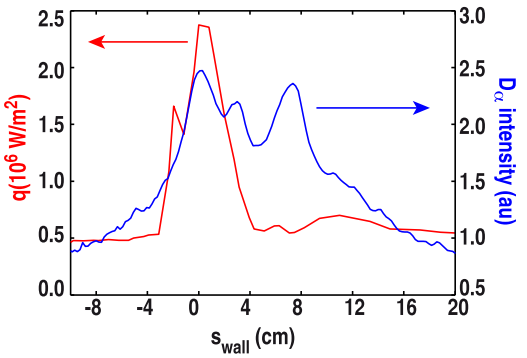

FIG. 4. Heat flux (red line) and D_α intensity (blue line) profiles at 3000 ms for discharge #129 194 at toroidal angle $\phi = 150°$. s_{wall} measures the distance from the inner strike point location on the target.

lobe at $s_{wall} = 5$ cm and in the broad SOL pattern within $s_{wall} = 8 - 10$ cm is detected. The level of heat flux arriving into these outer lobe structures is connected to a temperature drop at the pedestal. In the case where a temperature drop is seen, an increased heat flux is found in the outer lobes as seen in Fig. 2 for $3.45 < q_{95} < 3.55$ at $4.0 < s_{wall} < 6.0$ cm. This suggests a direct connection between a given point inside the separatrix and this outer lobe domain, which is also supported by a strong negative floating potential measured inside of the striated target flux patterns.[33] However, due to the uncertainty in analysis of plasma response and the complicated 3D transport processes in the perturbed edge, the exact radial domain connected from the interior of the plasma to the target cannot be quantified based on this measurement.[29] In fact, the existence of the striated pattern of particle flux and floating potential show clearly that invariant manifolds are formed. As they overlap at the X-point inside the separatrix,[5,34] these measurements show that this thin edge domain of $\Delta\psi_N = 1 - 3\%$ is opened to the wall. However, the parallel heat flux into the perturbed structures is much smaller than expected intuitively and also from 3D plasma fluid and kinetic neutral transport modeling even when screening out to the very edge is included.[35]

III. VACUUM APPROXIMATION

In the so called vacuum approximation, only the externally applied magnetic fields are taken into account. For the following analysis of drift effects, we use this paradigm for reference, being aware that plasma response effects are important. They will be taken into account in a next analysis step. Any magnetic field can be described by a Hamiltonian through the Clebsch form.[6] Therefore, the field lines, which are three dimensional curves tangent to the magnetic field $\boldsymbol{B}$, are described by a set of ordinary differential equations.

In a cylindrical coordinate system (R, φ, Z), the field line differential equations are

$$\frac{dR}{d\varphi} = R\frac{B_R}{B_\varphi}, \tag{1}$$

$$\frac{dZ}{d\varphi} = R\frac{B_Z}{B_\varphi} \tag{2}$$

with the total magnetic field $\boldsymbol{B}(R, \varphi, Z) = B_R\boldsymbol{e_R} + B_\varphi\boldsymbol{e_\varphi} + B_Z\boldsymbol{e_Z}$. The total magnetic field splits into the equilibrium part, which for DIII-D is given by an equilibrium (EFIT) reconstruction, and the perturbation part which is the superposition of the magnetic fields generated by the RMP coils and the intrinsic error fields. In DIII-D, the latter is mostly due to the poloidal field coils. The field from the RMP coils is directly calculated from the coil geometry using a Biot-Savart integration and the applied coil currents (typically 4 kA in the I-coil and 1 kA in the C-coil).

By solving Eqs. (1) and (2), we can trace field lines from a rectangular grid of initial conditions uniformly distributed in the poloidal/toroidal directions on the inner target region to generate a connection length footprint, as shown in Fig. 1(b). Each field line is traced for 500 toroidal turns or until it intersects with the vessel wall. The color gives the length of the field line inside the vessel, the connection length. In Fig. 1(b), a typical inner target footprint for discharge #132 741 is shown. The x-axis is given by the left-handed toroidal angle $\phi = (2\pi - \varphi)180/\pi$, as used for the DIII-D vessel; the y-axis is a length parameter t, which is measured along the vessel wall with $t = 0$ at the connection point of the 45° tile with the vertical centerpost and $t < 0$ on the centerpost; see Fig. 1(a) for details about the lower divertor region in DIII-D. Note that s_{wall} measures the length along the vessel wall relative to the SP position t_{SP}, while t is a fixed coordinate; it is $s_{wall} = t_{SP} - t$. The footprint pattern, here at 3000 ms, has the typical three-finger structure as generated by an $n = 3$ I-coil perturbation. But note that also $n = 1$ and $n = 2$ modes from the C-coil and intrinsic error fields are included. Each finger is actually infinite in length and continues periodically while converging towards the strike point with decreasing angle ϕ.

During the discharge, the edge safety factor q_{95} is ramped down, which causes the footprint pattern to change and rotate.[29] This way the footprint pattern can be moved toroidally in front of a stationary diagnostic like an IR camera. Looking at a fixed toroidal angle of $\phi = 150°$, we determine the position and width of each finger in the footprint pattern with changing q_{95}. Here, the width is determined by the position of the perturbed separatrix envelope, i.e., the boundary between field lines circulating in the plasma interior and connecting the divertor elements in the SOL. The result is shown in Fig. 3. Each line style (solid, dashed or dot-dashed) represents one of the fingers center, while the grey area gives the width of the finger at that point. Note that with increasing time q_{95} decreases. Hence, the time direction in Fig. 3 goes from right to left. With increasing q_{95}, the fingers in the footprint rotate in negative ϕ direction, which causes the finger tips to leave the toroidal observation window at some point. Once this happens, the finger reappears in a discontinuous manner at a different s_{wall} positions. But there is no discontinuity, because we only record the position and width of the outermost part of a finger

At first glance, the pattern shown in Fig. 3 shows similarities to the CII emission measurement in Fig. 2(b). A detailed comparison reveals that the vacuum prediction matches the measurement within reasonable limits, if the overall position of the stripe location pattern is shifted upwards by about 1 cm. The same holds for the outer part of the heat flux pattern, where only in selected q_{95} windows a significant heat flux arrives at the target plates above $s_{wall} = 2$ cm. However, as discussed before, the dominant part of the heat flux pattern, below $s_{wall} = 2$ cm, does not agree with the vacuum prediction at all and cannot be explained by it. A dominant heat inflow at the position of the unperturbed strike line is seen, which we attempt to understand in the following by adding particle drift effects to the differential equations of the magnetic field lines.

IV. ION DRIFT AND HEAT FLUX MODELLING

In a first step for extending the vacuum approximation, drift effects of electrons and ions are introduced, which follow the externally applied field. A self-consistent feedback

of the plasma particles onto the fields is neglected for now, but will be considered in future analysis (Sec. V). Due to gradients and curvature in the external magnetic fields, electrons and ions drift while gyrating along the field lines.

To include particle drift motion, the equations of motion for the field lines, Eqs. (1) and (2), have to be extended. Let us consider a particle with mass m_0 and charge $Z_q e$ ($Z_q = -1$ and $m_0 = m_e$ for electrons; $Z_q = +1$ and $m_0 = m_i$ for ions), where e is the elementary charge. The electromagnetic field is described by the magnetic vector potential $\vec{A}$ and the electric scalar potential $\hat{\phi}$. The vector potential includes the magnetic equilibrium field as well as the perturbation field, while the scalar potential describes any electric field. For simplicity, we neglect electric fields and set $\hat{\phi} = 0$, but electric fields might play a role, as can be seen from the discussion at the end of Sec. V, and will be included in future considerations.

We follow the derivation of the Hamiltonian drift equations as shown in Ref. 19, which are fully relativistic, but then obtain the non-relativistic limit since the kinetic energy of thermal ions is much smaller than the rest energy. Using the cylindrical coordinates $(\hat{R}, \varphi, \hat{Z})$ and time t, the relativistic particle Hamiltonian $\hat{H}$ can be formulated in standard form

$$\hat{H} = \left[c^2 \left(\hat{p}_R - \frac{Z_q e}{c} A_R \right)^2 + \frac{c^2}{\hat{R}^2} \left(\hat{p}_\varphi - \frac{Z_q e}{c} \hat{R} A_\varphi \right)^2 + c^2 \left(\hat{p}_Z - \frac{Z_q e}{c} A_Z \right)^2 + m_0^2 c^4 \right]^{1/2}. \tag{3}$$

By applying a zeroth order guiding-center approximation, which means we essentially average over the fast-varying gyro-phase ϑ_x, we transform from the fast-varying coordinates $(\hat{R}, \varphi, \hat{Z}, t, p_R, p_\varphi, p_Z, p_t = -\hat{H}/m_0\omega_c^2 R_0^2)$ to the slowly-varying guiding-center coordinates $(x_c, \varphi, z_c, t, I_x, p_\varphi, p_z, p_t)$. For passing particles, the Hamiltonian drift equations can be reformulated by introducing the toroidal angle φ as the independent, time-like variable and the corresponding canonical momentum p_φ as a new Hamiltonian $K = -p_\varphi$, i.e.,

$$K = -f_\varphi + \sigma(1 + x_c)\left[\varepsilon_0(\gamma^2 - 1) - 2\omega_x I_x\right]^{1/2} \tag{4}$$

with the relativistic factor $\gamma = -p_t/\varepsilon_0 = 1 + E_{kin}/m_0 c^2$, the normalized particle rest energy $\varepsilon_0 = c^2/\omega_c^2 R_0^2$, the gyro frequency $\omega_c = eB_0/m_0 c$ due to the main toroidal magnetic field B_0 at the magnetic axis, the normalized particle gyro-frequency $\omega_x = 1/(1 + x_c) = e^{p_z/Z_q}$, and the normalized vector potential component $f_\varphi = Z_q(1 + x_c)A_\varphi/B_0 R_0$. The parameter σ determines the direction of motion along the field line relative to the toroidal angle. σ is $+1$ for co-passing (counter-clockwise) and -1 for counter-passing (clockwise) particles. For $\sigma = 0$, we recover the field line equations, Eqs. (1) and (2).

The term $\varepsilon_0(\gamma^2 - 1)$ is the only part of the Hamiltonian K, which depends on the normalized total particle energy p_t. For the non-relativistic limit, we have to separate the non-relativistic part of the energy from the total relativistic energy by subtracting the rest energy, introducing the non-relativistic canonical momentum $h = -p_t - \varepsilon_0 = E_{kin}/m_0\omega_c^2 R_0^2$. At the non-relativistic limit, the kinetic energy is much smaller than the rest energy. So, we define $\mu := h/\varepsilon_0 \ll 1$ and expand the relevant term into a power series with respect to μ

$$\varepsilon_0(\gamma^2 - 1) \approx 0 + 2\varepsilon_0\mu + O(\mu^2) = 2h \tag{5}$$

and neglect all higher orders of μ. Inserting this result into the relativistic Hamiltonian K, we get the non-relativistic Hamiltonian

$$K_{nr} = -f_\varphi - \sigma(1 + x_c)[2(h - \omega_x I_x)]^{1/2}. \tag{6}$$

The particle drift orbits are then described by the Hamiltonian equations of motion

$$\frac{dz_c}{d\varphi} = \frac{1}{Z_q}(1 + x_c)\left[\frac{\partial f_\varphi}{\partial x_c} - \sigma(2h - \omega_x I_x) \times (2(h - \omega_x I_x))^{-1/2}\right], \tag{7}$$

$$\frac{dp_z}{d\varphi} = \frac{\partial f_\varphi}{\partial z_c}, \tag{8}$$

$$\frac{dt}{d\varphi} = -\sigma(1 + x_c)(2(h - \omega_x I_x))^{-1/2}, \tag{9}$$

$$\frac{dh}{d\varphi} = \frac{\partial f_\varphi}{\partial t}, \tag{10}$$

$$\frac{d\vartheta_x}{d\varphi} = -\sigma[2(h - \omega_x I_x)]^{-1/2}, \tag{11}$$

$$\frac{dI_x}{d\varphi} = 0. \tag{12}$$

Transforming Eqs. (7) and (8) back into non-dimensionless (physical) coordinates, we find

$$\frac{dR}{d\varphi} = R\frac{B_R}{B_\varphi}, \tag{13}$$

$$\frac{dZ}{d\varphi} = R\frac{B_Z}{B_\varphi} - \frac{\sigma}{Z_q}\left[RS(R) + \frac{R_0 I_x}{S(R)}\right] \tag{14}$$

with

$$S(R) = \sqrt{2(h - R_0 I_x/R)}. \tag{15}$$

For the parameters we have the major radius of the tokamak $R_0 = 1.7$ m, the toroidal magnetic field at the major radius $B_0 = 1.79$ T, as in discharge #129 194 ($B_0 = 1.84$ T in #132 741). I_x is obviously a constant of motion and can be estimated as $I_x \approx -\varepsilon_0[(\lambda(\gamma - 1) + 1)^2 - 1]/(2Z_q)$ with the relative energy $\lambda = E_\perp/E_{kin}$, associated with the particle motion perpendicular to the magnetic field line. It has been numerically checked that the shift of the drift surfaces with respect to the magnetic flux surfaces only depends very weakly on λ; the modification is within a few percent for λ between 0.1 and 0.9. So, without limiting the result of the

model, we use $\lambda = 0.1$ here. Note that the guiding center equations (13) and (14) only describe passing particles; trapping effects are neglected. Typically, particles coming from the outer midplane region see a substantial mirror ratio on their way towards the inner divertor. To avoid this issue, we launch all drift orbit traces directly from the inner target plate. Since we are only interested in the flux that arrives at the inner target plate, only particles moving towards the inner target are relevant, i.e., co-passing ions and counter-passing electrons. For such particles the orbit trace is reverse with respect to the particle motion, and each orbit we trace, contributes to the flux towards the inner target.

Besides the particle species and the direction of motion, the drift motion depends on the particle kinetic energy E_{kin}. According to fundamental drift theory, the drift velocity in inhomogeneous magnetic fields reads $v_{Drift} = 4E_{kin}(\vec{B} \times \nabla B)/3Z_q eB^3$. So, the higher the kinetic energy, the more the drift orbit deviates from the field line as shown in Ref. 36 for ions and in Ref. 19 for electrons. On the same orbit, the drift velocity of ions and electrons is the same for equal kinetic energies, but the electron parallel velocity $v_{\|,e}$ (velocity along the orbit) is $\sqrt{m_i/m_e}$ times higher than the ion parallel velocity $v_{\|,i}$. The time dT to move the distance $ds = v_{\|}dT$ along the orbit is therefore $\sqrt{m_i/m_e}$ times longer for ions than for electrons, in which the particles drift away from the field lines with the same drift velocity. As a result, at similar energies ion orbits deviate much more from field lines than electron orbits.

In the following, we consider only thermal particles. At typical plasma temperatures of about 1–2 keV in DIII-D, the Maxwellian energy distribution contains relevant kinetic energies between 0 and 18 keV. Within this energy range, the electron orbit deviation from the field line is negligible; the ion orbit deviation is not. This means that in the following, we only consider drifting ions, while treating electrons like field lines.

Using the following procedure, we can simulate the heat flux to the inner divertor target in DIII-D.

(1) We sample the normalized Maxwellian energy distribution (normalized as a probability distribution with $\int_0^\infty p(E)\,dE = 1$)

$$p(E) = \frac{1}{(k_B T_i)^2} E e^{-E/k_B T_i} \tag{16}$$

at a plasma temperature of $k_B T_i = 2$ keV with energies $E = 0.25, 0.5, ..., 17.75, 18$ keV and $\Delta E = 0.25$ keV.

(2) For each energy in the sample, we simulate the penetration depth (ψ_{Min}) footprint (e.g., Fig. 3 in Ref. 34), which shows the minimum of normalized flux ψ an ion reaches on its way from the outer target to the inner target. Note that this footprint shows the same features as a connection length (L_c) footprint, like, e.g., Fig. 1(b). The footprint is obtained by tracing a large number of co-passing, i.e., $\sigma = +1$, ion drift trajectories, originating from a rectangular (ϕ, θ) grid on the inner divertor target, backwards into the plasma and eventually to the outer divertor target. Since only ions which are moving towards the inner target can contribute to the heat flux, we only need to consider co-passing ions; counter passing ions would move away from the inner target, back into the plasma. So remember that the trace of the ion trajectories is reverse with respect to the ion motion.

(3) Using an axisymmetric, flux-surface-averaged ion temperature profile $T_i(\psi)$ of the discharge, as, e.g., obtained through Charge Exchange Recombination (CER) Spectroscopy, we translate the penetration depth footprint into a temperature footprint by assigning $\psi_{Min} \rightarrow T_i(\psi_{Min})$, and then replace the temperature with the mean energy $3/2k_B T_i$ of the corresponding Maxwellian distribution. In the resulting *energy footprint*, we only keep the part of the footprint where it agrees with the energy level E, within a ΔE range, for which the footprint was simulated. This way we keep only those ion orbits that carry the energy E to the inner target.

(4) The remaining energy footprint parts for the various energies E are superimposed, weighting them with their respective contribution to the Maxwellian distribution $p(E)\Delta E$. Because every point in the superimposed pattern resembles one ion, the resulting footprint pattern is a spatial average of the energy per ion $\langle E \rangle$ on the target.

(5) The average energy $\langle E \rangle$ pattern can easily be recalculated into a heat flux q pattern using the thermal velocity v_{th} and a typical ion density n_i by

$$q = \frac{1}{2} n_i v_{th} \langle E \rangle = \frac{1}{2} n_i \sqrt{\frac{k_B T_i}{m_i}} \langle E \rangle. \tag{17}$$

This linear model assumes a fully Maxwellian energy distribution of ions and does not include sheath heat transmission effects and the impact of non-Maxwellian particle transfer at the sheath-wall interface. Within the usual discussion on how accounting for the sheath heat transmission physics (e.g., Ref. 37 and application to measurements with RMP ELM suppression in Ref. 33), the electron heat flux is calculated as $q_e = \gamma_e \Gamma T_e$ with $\Gamma = n_e c_s$ and the sheath heat transmission coefficient γ_e for electrons, which can be ~5 or more. Since we are not including sheath heat transmission effects in the presented model so far, we are implicitly assuming a sheath heat transmission coefficient $\gamma_i = 1$ for ions here. The actual value of this factor would scale our results linearly when comparing absolute magnitudes of heat fluxes between measurement and our model.

(6) A small-span simple moving average filter is applied to smooth over some of the very high frequency fluctuations in the resulting heat flux pattern.

The solid line in Fig. 5 shows the profile of the simulated heat flux pattern at a toroidal angle $\phi = 150°$ at 3000 ms in discharge #129 194. The dashed line is the field line connection length profile. Note that the latter is not smoothed and therefore still has a partly stochastic structure. The field line profile shows how the heat flux profile would look like according to the vacuum approximation without drifts and also represents the electron flux profile. Both patterns are significantly different from each other. The heat flux profile is shifted about 2 cm towards the private flux region compared

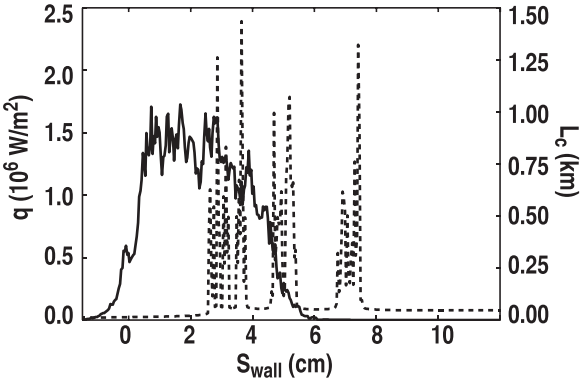

FIG. 5. Modelled heat flux (sold line) and field line connection length (dashed line) profiles at 3000 ms for discharge #129 194 at toroidal angle $\phi = 150^{\circ}$. s_{wall} measures the distance from the inner strike point location on the target.

to the field line pattern and shows no typical $n = 3$ RMP striation as expected from the field line connection length profile. The calculated heat flux has a peak value of about 1.75×10^6 W/m^2 and a pattern width of about 5 cm. There is a reasonable agreement with the measured heat flux pattern for this discharge as shown in Fig. 4. The calculated peak heat flux is only about 24% smaller than the measured one, while the pattern width and characteristic feature, one single peak with no RMP striation, are well reproduced. As discussed above, sheath heat transmission effects are not part of the model so far, implying an ion transmission coefficient of 1. Changing the latter could scale the height of the simulated heat flux, although it is already within reasonable quantitative agreement with the measurement. Further investigation on this matter will be done in the future. Also, as discussed in Ref. 31, the upstream ion temperature inside of the plasma which determines the energy distribution applied in this drift model is dependent on q_{95} which is not taken into account here.

Within the drift approach, the field line connection length profile also represents the electron flux profile (in arbitrary units of course), while the ion flux profile proportionally agrees with the calculated heat flux profile. Combining both to a total particle flux profile shows similarities to the measured D_α intensity profile, given by the blue line in Fig. 4. However, the non-ambipolar transport effects at the sheath entrance and inside the sheath, if electrons and ions are separated like this at the plate, are not accounted for here. This is matter of ongoing work. The combined profile of electrons and ions from this solution would also exhibit a three peak profile due to the electron contribution with a pattern width of about 8 cm, which is much closer to the maximum total profile width of about 9 cm, measured by CII emission during q_{95} ramp down as shown in Fig. 2.

V. SIMULATED HEAT FLUX

To further test the importance of particle drifts in H-mode plasmas and to provide more confidence in the proposed model, we now apply the model to discharge #132 741. As mentioned in Sec. II, this discharge has a q_{95} ramp where q_{95} goes from 4.01 at 2670 ms to 3.3 at 4250 ms. Due to the q_{95} ramp, the magnetic structure changes, including the footprint patterns, as discussed in Ref. 29 and in Sec. III. Therefore, the calculated heat flux pattern changes with q_{95}; the footprint of a fixed energy ion drift pattern varies in the same manner as the field line pattern and looks quite similar to it apart from the difference between both due to the drift effect, which is independent of q_{95} as far as the magnetic topology is concerned. The q_{95} dependent ion temperature distribution is of order $10\% - 50\%$.[31] The difference in the overall drift behavior is expected to be insignificant on the level of first time exploration of drift effects discussed in this paper.

Calculating the heat flux for various time slices, we find a fair agreement between the measured and the calculated heat flux, as shown in the four different cases in Fig. 6. The main heat flux peak (or peaks as in the 4250 ms case) is always well reproduced. The characteristic shape, which lacks the $n = 3$ striation, of the heat flux measurements is a robust feature of the model. The peak value with $\gamma = 1$ can deviate up

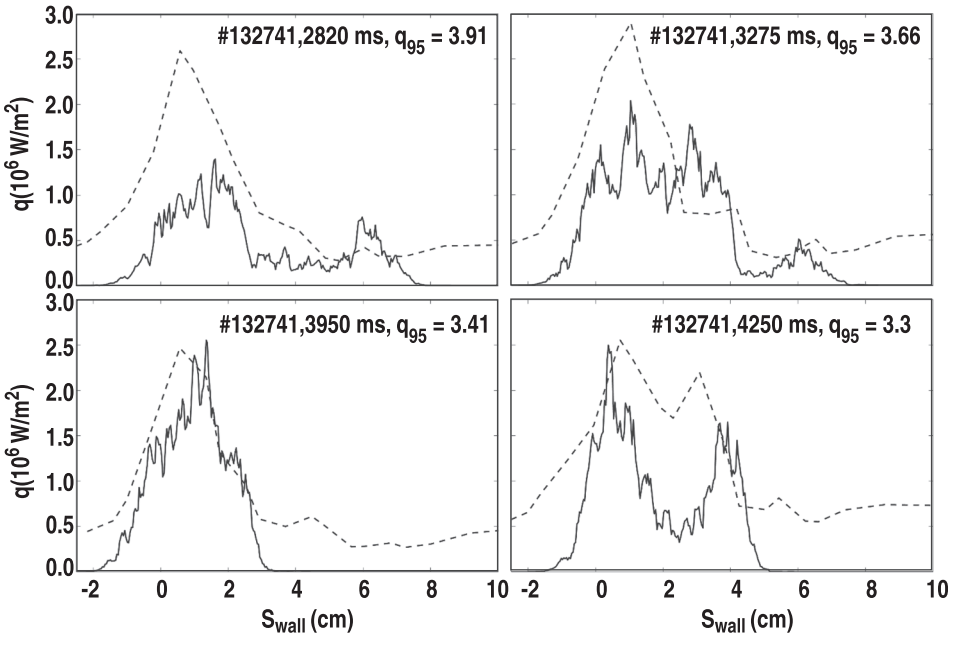

FIG. 6. Comparison of modelled heat flux q (sold line) and measured heat flux (dashed line) profiles at various times within discharge #132 741 at toroidal angle $\phi = 150^{\circ}$. s_{wall} measures the distance from the inner strike point location on the target.

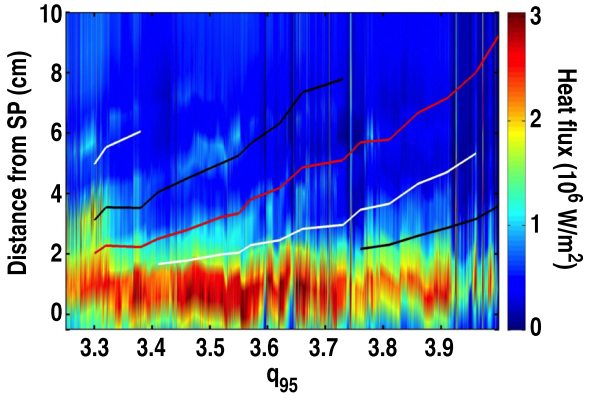

FIG. 7. Same as Fig. 1(a) but including the 1 cm shifted positions of the field line connection length footprint finger's centres as shown in Fig. 4. Each line color corresponds to one finger.

to 40%, as shown in the 2820 ms case, but is much closer to the other measured cases. This can be matter of the q_{95} dependent ion temperatures at the upstream position discussed beforehand. The radial position on the target and the width of the main peak is always in good agreement with the measurements. In two cases (top row), small heat flux peaks further away from the strike point position, $s_{wall} = 0$, are reproduced by the model as well, while they are missing in the other two cases (bottom row). A possible reason for this is the contribution of electrons to the heat flux, discussed below.

So far we completely neglected any influence of electrons. There are two contributions which are discussed in the following. First, the electrons themselves can directly contribute to the measured heat flux. Second, the individual treatment of electrons and ions and their significantly different drift behaviour leads to a charge separation which is unaccounted for in this model. Such a charge separation introduces ambipolar electric fields, which themselves act back onto the electron and ion motion. It is possible to calculate such ambipolar fields self-consistently and include them into the drift equations (13) and (14), as was shown in previous publications.[38–40] Extending the proposed model to include self-consistent ambipolar electric fields will be part of future work though.

Combining the analysis of the finger position in the vacuum case (Fig. 3) which also represents the electrons, with the heat flux measurement, Fig. 2(a), shows that the outermost weak striation patterns line up quite well with the finger positions, if the finger position is shifted by about 1 cm away from the private flux region, as shown in Fig. 7. Note that the shift predicted by the model is about 2 cm. This leads to two conclusions within the proposed model. First, thermal electrons follow the field lines quite well and contribute to the measured heat flux, but less than a factor of 3 or higher. Second, most likely due to ambipolar electric fields, which are not yet included in the model, the separation between electrons and ions is reduced to about 50% of the predicted shift.

VI. CONCLUSIONS

Heat flux and particle flux patterns related (CII emission and D_α intensity) measurements in low-collisionality H-mode plasmas were analysed. Both patterns significantly differ from each other. A comparison of the observed striation in CII emission as well as D_α intensity measurements during RMPs with magnetic connection length footprints, calculated by vacuum field line tracing, shows strong geometrical similarities. Both agree within reasonable limits as far as the position of the striation is concerned, provided the calculated overall pattern is shifted by about 1 cm away from the private flux region. On the other hand, the measured heat flux is dominated by a single large heat flux peak, located at the position of the unperturbed strike point.

To explain the differences between the two measurements and the heat flux itself, a drift model was introduced which includes the guiding center drift motion of passing particles into the equations of motion. Thermal electrons show no significant deviation from magnetic field lines, while thermal ions, depending on their kinetic energy, can drift several cm away from a magnetic field line. A procedure to calculate the heat influx onto the target from ion drift motion was applied to the discussed discharges. Good agreement was found for several cases of different edge safety factors. The qualitative shapes and positions of the modeled and measured heat flux profiles match well. The calculated heat flux magnitude agrees in most cases with the measured one as well. However, there is still room for refinement since no sheath transmission model was applied and q_{95} dependent changes of the upstream ion temperature have not yet been accounted for.

The considered discharges are characterized by low collisionality, which means we can expect the effect of collisions to be small. The model neglects collision effects and assumes the collision-free limit. In EMC3/EIRENE simulations for various perpendicular diffusion coefficients, it is found that high radial diffusive transport yields a smear out of the magnetic field line target pattern. Reduction in radial diffusion concentrates the fluxes along the open field lines back into the pattern of the magnetic topology.[29] Taking the low collisionality into account, we would expect a similar small smear out behavior for the patterns calculated by our model. For high collisionality, it is experimentally observed though that the heat flux forms a striated pattern similar to the particle flux. This collisionality dependence is not yet covered by our model but will be investigated in the future.

The role of electrons was briefly discussed. We found that within the framework of the model, thermal electrons follow the field lines quite well and create the striated part of the heat flux pattern, which has at least 67% lower intensity.

Also the possible influence of ambipolar electric fields, as generated by the charge separation between electrons and ions, was discussed, but a generalization of the model to include such fields and a corresponding detailed analysis is planned for future work. Future work also involves sensitivity scans with respect to the parameters used here, but preliminary observations indicate that, e.g., changing n_i or T_i leaves the profile shape rather unaffected while scaling the magnitude of the simulated heat flux. Including further plasma response effects, e.g., screening, will not necessarily improve the model. A preliminary study suggests that massive screening shrinks the RMP strike point splitting and

therefore worsens the agreement to the CII emission as well as D_α intensity measurements. On the other hand, including more sheath physics is part of planned improvements.

ACKNOWLEDGMENTS

This work was supported by the US Department of Energy under DE-AC05-00OR22725 and DE-FC02-04ER54698, as well as the DFG under Project No. SP229/1-1. Discussions with R. Maingi and D. N. Hill are gratefully acknowledged.

[1]H. Zohm, Plasma Phys. Controlled Fusion **38**, 1213 (1996).
[2]ITER Physics Basis Editors, ITER Physics Expert Group Chairs and Co-Chairs, and ITER Joint Central Team and Physics Integration Unit, Nucl. Fusion **39**, 2137 (1999).
[3]A. Loarte, G. Saibene, R. Sartori, D. Campbell, M. Becoulet, L. Horton, T. Eich, A. Herrmann, G. Matthews, N. Asakura, A. Chankin, A. Leonard, G. Porter, G. Federici, G. Janeschitz, M. Shimada, and M. Sugihara, Plasma Phys. Controlled Fusion **45**, 1549 (2003).
[4]T. E. Evans, R. A. Moyer, K. H. Burrell, M. E. Fenstermacher, I. Joseph, A. W. Leonard, T. H. Osborne, G. D. Porter, M. J. Schaffer, P. B. Snyder, P. R. Thomas, W. P. West, and J. G. Watkins, Nat. Phys. **2**, 419 (2006).
[5]O. Schmitz, T. E. Evans, M. E. Fenstermacher, A. McLean, J. Boedo, N. H. Brooks, H. Frerichs, M. Jakubowski, R. Laengner, C. L. Lasnier, A. Loarte, R. A. Moyer, D. Orlov, H. Reimerdes, D. Reiter, U. Samm, H. Stoschus, E. A. Unterberg, J. G. Watkins, and DIII-D and TEXTOR Teams, J. Nucl. Mater. **415**, S886–S893 (2011).
[6]R. Balescu, *Matter out of Equilibrium* (Imperial College Press, London, 1977).
[7]R. Balescu, *Aspects of Anomalous Transport in Plasmas* (Institute of Physics Publishing, Bristol, 2005).
[8]K. H. Finken, S. S. Abdullaev, W. Biel, M. F. M. de Bock, C. Busch, E. Farshi, M. von Hellermann, G. M. D. Hogeweij, M. Jakubowski, R. Jaspers, H. R. Koslowski, A. Kraemer-Flecken, A. Lazaros, M. Lehnen, Y. Liang, A. Nicolai, O. Schmitz, B. Unterberg, E. Westerhof, R. Wolf, O. Zimmermann, M. de Baar, G. Bertschinger, S. Brezinsek, I. G. J. Classen, A. J. H. Donné, H. G. Esser, H. Gerhauser, B. Giesen, D. Harting, J. A. Hoekzema, P. W. Huettemann, S. Jachmich, K. Jakubowska, D. Kalupin, F. Kelly, Y. Kikuchi, A. Kirschner, R. Koch, M. Korten, A. Kreter, J. Krom, U. Kruezi, A. Litnovsky, X. Loozen, N. J. L. Cardozo, A. Lyssoivan, O. Marchuk, P. Mertens, A. Messiaen, O. Neubauer, V. Philipps, A. Pospieszczyk, D. Reiser, D. Reiter, A. L. Rogister, T. V. Rompuy, A. Savtchkov, U. Samm, R. P. Schorn, F. C. Schueller, B. Schweer, G. Sergienko, K. H. G. Telesca, M. Tokar, G. V. Oost, R. Uhlemann, G. V. Wassenhove, R. Weynants, S. Wiesen, and Y. Xu, Plasma Phys. Controlled Fusion **46**, B143–B155 (2004).
[9]M. Lehnen, S. Abdullaev, W. Biel, M. F. M. de Bock, S. Brezinsek, C. Busch, I. Classen, K. H. Finken, M. von Hellermann, S. Jachmich, M. Jakubowski, R. Jaspers, H. R. Koslowski, A. Krämer-Flecken, Y. Kikuchi, Y. Liang, A. Nicolai, A. Pospieszczyk, T. V. Rompuy, U. Samm, O. Schmitz, G. Sergienko, B. Unterberg, R. Wolf, O. Zimmermann, and TEXTOR Team, Plasma Phys. Controlled Fusion **47**, B237–B248 (2005).
[10]M. W. Jakubowski, S. S. Abdullaev, K. H. Finken, M. Lehnen, and TEXTOR Team, J. Nucl. Mater. **337–339**, 176 (2005).
[11]M. W. Jakubowski, A. Wingen, S. S. Abdullaev, K. H. Finken, M. Lehnen, K. H. Spatschek, R. C. Wolf, and TEXTOR Team, J. Nucl. Mater. **363–365**, 371 (2007).
[12]A. Wingen, M. W. Jakubowski, K. H. Spatschek, S. S. Abdullaev, K. H. Finken, M. Lehnen, and TEXTOR Team, Phys. Plasmas **14**, 042502 (2007).
[13]O. Schmitz, D. Harting, S. S. Abdullaev, S. Brezinsek, K. H. Finken, H. Frerichs, M. Jakubowski, M. Lehnen, X. Loozen, P. Mertens, D. Reiter, U. Samm, B. Schweer, G. Sergienko, M. Z. Tokar, B. Unterberg, R. C. Wolf, and TEXTOR Team, J. Nucl. Mater. **363–365**, 680 (2007).
[14]D. Harting, D. Reiter, Y. Feng, O. Schmitz, D. Reiser, and H. Frerichs, Contrib. Plasma Phys. **48**, 99 (2008).
[15]H. Stoschus, M. Lehnen, O. Schmitz, D. Reiser, B. Unterberg, U. Samm, and TEXTOR Team, Nucl. Fusion **53**, 012001 (2013).
[16]H. Stoschus, O. Schmitz, B. Unterberg, M. W. Jakubowski, H. Frerichs, U. Kruezi, D. Reiter, and U. Samm, J. Nucl. Mater. **415**, S923 (2011).
[17]D. Reiser and D. Chandra, Phys Plasmas **16**, 042317 (2009).
[18]J. Wesson, *Tokamaks* (Clarendon Press, Oxford, 2004).
[19]A. Wingen, S. S. Abdullaev, K. H. Finken, and K. H. Spatschek, Nucl. Fusion **46**, 941 (2006).
[20]T. E. Evans, R. A. Moyer, and P. Monat, Phys. Plasmas **9**, 4957 (2002).
[21]R. K. W. Roeder, B. I. Rapoport, and T. E. Evans, Phys Plasmas **10**, 3796 (2003).
[22]T. E. Evans, R. K. Roeder, J. A. Carter, B. I. Rapoport, M. E. Fenstermacher, and C. J. Lasnier, J. Phys.: Conf. Ser. **7**, 174 (2005).
[23]A. Wingen, T. E. Evans, and K. H. Spatschek, Phys. Plasmas **16**, 042504 (2009).
[24]O. Sauter, C. Angioni, and Y. R. Lin-Liu, Phys. Plasmas **6**, 2834 (1999).
[25]J.-W. Ahn, J. M. Canik, V. A. Soukhanovskii, R. Maingi, and D. J. Battaglia, Nucl. Fusion **50**, 045010 (2010).
[26]J.-W. Ahn, R. Maingi, J. M. Canik, A. G. McLean, J. D. Lore, J.-K. Park, V. A. Soukhanovskii, T. K. Gray, and A. L. Roquemore, Phys Plasmas **18**, 056108 (2011).
[27]I. Joseph, T. Evans, A. Runov, M. Fenstermacher, M. Groth, S. Kasilov, C. Lasnier, R. Moyer, G. Porter, M. Schaffer, R. Schneider, and J. Watkins, Nucl. Fusion **48**, 045009 (2008).
[28]H. Frerichs, D. Reiter, O. Schmitz, T. E. Evans, and Y. Feng, Nucl. Fusion **50**, 034004 (2010).
[29]O. Schmitz, T. E. Evans, M. E. Fenstermacher, H. Frerichs, M. W. Jakubowski, M. J. Schaffer, A. Wingen, W. P. West, N. Brooks, K. H. Burrell, J. deGrassie, Y. Feng, K. H. Finken, P. Gohil, M. Groth, I. Joseph, C. J. Lasnier, M. Lehnen, A. W. Leonard, S. Mordijck, R. A. Moyer, A. Nicolai, T. Osborne, D. Reiter, U. Samm, K. H. Spatschek, H. Stoschus, B. Unterberg, E. A. Unterberg, J. G. Watkins, R. Wolf, and DIII-D and TEXTOR Teams, Plasma Phys. Controlled Fusion **50**, 124029 (2008).
[30]O. Schmitz, T. E. Evans, M. E. Fenstermacher, E. A. Unterberg, M. E. Austin, B. D. Bray, N. H. Brooks, H. Frerichs, M. Groth, M. W. Jakubowski, C. J. Lasnier, M. Lehnen, A. W. Leonard, S. Mordijck, R. A. Moyer, T. H. Osborne, D. Reiter, U. Samm, M. J. Schaffer, B. Unterberg, W. P. West, and DIII-D and TEXTOR Research Teams, Phys. Rev. Lett. **103**, 165005 (2009).
[31]O. Schmitz, T. E. Evans, M. E. Fenstermacher, M. Lehnen, H. Stoschus, E. A. Unterberg, J. W. Coenen, H. Frerichs, M. W. Jakubowski, R. Laengner, C. L. Lasnier, S. Mordijck, R. A. Moyer, T. H. Osborne, H. Reimerdes, D. Reiter, U. Samm, B. Unterberg, and DIII-D and TEXTOR Teams, Nucl. Fusion **52**, 043005 (2012).
[32]M. W. Jakubowski, T. E. Evans, M. E. Fenstermacher, M. Groth, C. J. Lasnier, A. W. Leonard, O. Schmitz, J. G. Watkins, T. Eich, W. Fundamenski, R. A. Moyer, R. C. Wolf, L. B. Baylor, J. A. Boedo, K. H. Burrell, H. Frerichs, J. S. deGrassie, P. Gohil, I. Joseph, S. Mordijck, M. Lehnen, C. C. Petty, R. I. Pinsker, D. Reiter, T. L. Rhodes, U. Samm, M. J. Schaffer, P. B. Snyder, H. Stoschus, T. Osborne, B. Unterberg, E. Unterberg, and W. P. West, Nucl. Fusion **49**, 095013 (2009).
[33]J. G. Watkins, T. E. Evans, M. Jakubowski, R. A. Moyer, O. Schmitz, A. Wingen, M. E. Fenstermacher, I. Joseph, C. J. Lasnier, and D. L. Rudakov, J. Nucl. Mater. **390–391**, 839–842 (2009).
[34]A. Wingen, T. E. Evans, and K. H. Spatschek, Nucl. Fusion **49**, 055027 (2009).
[35]H. Frerichs, D. Reiter, O. Schmitz, P. Cahyna, T. E. Evans, Y. Feng, and E. Nardon, Phys Plasmas **19**, 052507 (2012).
[36]S. S. Abdullaev, A. Wingen, and K. H. Spatschek, Phys. Plasmas **13**, 042509 (2006).
[37]P. C. Stangeby, *The Plasma Boundary of Magnetic Fusion Devices* (Institute of Physics Publishing, 2000).
[38]A. Wingen and K. H. Spatschek, Phys. Plasmas **15**, 052305 (2008).
[39]A. Wingen and K. H. Spatschek, Phys. Rev. Lett. **102**, 185002 (2009).
[40]A. Wingen and K. H. Spatschek, Nucl. Fusion **50**, 034009 (2010).